Choked accretion onto Kerr-Sen black holes in Einstein-Maxwell-dilaton-axion gravity

Haiyuan Feng,[1,*] Yingdong Wu,[1,‡] Rong-Jia Yang,[2,†] and Leonardo Modesto[1,§]
[1]Department of Physics, Southern University of Science and Technology, Shenzhen 518055, Guangdong, China
[2]College of Physical Science and Technology, Hebei University, Baoding 071002, China

(Received 28 September 2023; accepted 6 February 2024; published 12 March 2024)

We investigate the process of an ultrarelativistic fluid accreted onto axisymmetric Kerr-Sen black holes in Einstein-Maxwell-dilaton-axion theory. We obtain the solution describing the velocity potential of a stationary irrotational fluid with a stiff equation of state and the solution for the streamlined diagram of the quadrupolar flow. We also investigate how the solution's coefficients and the stagnation points are affected by the parameters. The injection rate, the ejection rate, and the critical angle are discussed in detail. We find that with an increasing dilaton parameter the ratio of the ejection rate to the injection rate increases and that the radiative efficiency is larger, while the redshift is lower, compared to the Kerr black hole.

DOI: 10.1103/PhysRevD.109.063014

I. INTRODUCTION

Accretion of matter onto a black hole is the most probable scenario for explaining the high-energy output from active galactic nuclei and quasars. It is also provides the most credible expositions for the high-energy outflow from x-ray binaries and gamma-ray bursts [1]. The initial exploration of accretion process onto celestial objects was investigated by Hoyle and Lyttleton [2–5]. Subsequently, Bondi and Hoyle focused on the accretion of gas without pressure onto a moving star [6]. Bondi formulated the theory of the transonic hydrodynamic accretion of the adiabatic fluid in a stationary, spherically symmetric spacetime [7]. This scheme for accretion process was generalized to the Schwarzschild black hole by Michel [8]. Petrich formulated a relativistic framework for the stationary accreted fluid with an adiabatic equation of state onto a Schwarzschild and Kerr black hole [9]. In recent developments, researchers considered the accretion of Vlasov gas, ignoring the backreaction of matter, and analyzed its accretion rate [10–12]. Since then, a considerable amount of literature has been dedicated to theoretical and observational studies for accretion [13–25]. On the flip side, the astrophysical jet represents another phenomenon, where plasma is emitted in the form of an extended beam along the rotation axis. The jet mechanisms proposed by Blandford and Payne (BP) and Blandford and Znajek (BZ) stand as the most widely accepted explanations in prior studies [26,27]. The BP mechanism utilizes magnetic centrifugation to extract energy and angular momentum from a black hole accretion disk, whereas the BZ mechanism involves rotational energy from a Kerr black hole. These methods were commonly used in magnetohydrodynamics and astrophysics explorations [28–31]. Afterward, a new hydrodynamic accretion mechanism was proposed to explain the effect of the steady-state axisymmetric partial fluid flowing from the equatorial plane being ejected along poles by the cytaster's gravitational influence [32]. This process was also generalized to the choked accretion scenario of Schwarzschild and Kerr black holes [33,34].

The preceding discussions were primarily confined to the general relativity (GR) framework. Similar accretion and jet phenomena exist for black holes in alternative gravity models [35–41]. In GR, the theoretical predictability is broken by singularities associated with black holes and by the big bang [42–44]. This suggests that GR may not be a complete theory of gravity, highlighting the necessity for modifications from a more comprehensive theory that incorporates the quantum nature at very small length scales [45]. From an observational standpoint, GR encounters challenges in understanding the characteristics of dark matter and dark energy, both essential for explaining phenomena such as the rotation curves of galaxies and the accelerated expansion of the Universe, respectively [46–50]. Furthermore, recent developments suggest a breakdown of GR in the low-acceleration regime, thereby exerting profound influence on both the astrophysical and cosmological domains [51,52].

Among many alternative theories to traditional GR, the Einstein-Maxwell-dilaton-axion (EMDA) model has attracted significant attention [53,54]. The model incorporates the dilaton field and the pseudoscalar axion, both of which are connected to the metric and the Maxwell field.

*Corresponding author: 406606114@qq.com
†Corresponding author: yangrongjia@tsinghua.org.cn
‡12131274@mail.sustech.edu.cn
§lmodesto@sustech.edu.cn

The origins of the dilaton and axion fields can be attributed to string compactifications, giving rise to compelling implications in the inflationary and late-time accelerated cosmologies [55,56]. Therefore, it is valuable to investigate the role of such a theory in astrophysical observations. Within these string-inspired low-energy effective theories, the parameters were constrained from observations; for instance, a preferred value of $r_2 \equiv \frac{Q^2}{M} \approx 0.2M$ is determined based on the optical continuum spectrum of quasars [57]. Additionally, a recent investigation gave an observational constraint on the dilaton parameter ($0.1M \lesssim r_2 \lesssim 0.4M$) by analyzing the shadow diameters of M87* and Sgr A* [58]. Finally, a constraint on the dilaton parameter is obtained by employing simulated data that replicates potential observations of the S2 star via a gravity interferometer [59]. It demonstrated that enhanced astrometric accuracy can effectively narrow down the acceptable range of dilaton parameter to $r_2 \lesssim 0.066M$.

The article is organized as follows: In Sec. II, the EMDA model and the Kerr-Sen black hole will be briefly reviewed. In Sec. III, for irrotational fluids, we will derive an analytical solution for the velocity potential Φ in the Boyer-Lindquist coordinate system. In Sec. IV, the quadrupolar flow solution will be used to analyze the variation of the coefficients with parameters, and the streamline and the temperature diagrams will be displayed in the zero angular momentum observer frame. In Sec. V, we will present the mechanism of choked accretion, including the density ratio, the injection rate, and the ejection rate, as well as the value range of the reference point. Finally, we will analyze the variation of radiative efficiency ϵ and redshift z with different parameters. For convenience, we will use geometrical units $c = G = 1$ and the signature convention $(-,+,+,+)$ for the spacetime metric throughout the article.

II. KERR-SEN BLACK HOLE IN EINSTEIN-MAXWELL-DILATON-AXION GRAVITY

The EMDA model is derived from the low-energy limit behavior of heterotic string theory. It is composed of dilaton field χ, gauge vector field A_μ, metric $g_{\mu\nu}$, and pseudoscalar axion field ξ [53,54,60]. The action of the EMDA model can be formulated through the coupling of supergravity and super-Yang-Mills theory, and it can be described by the following form:

$$S = \frac{1}{16\pi}\int \sqrt{-g}d^4x\Big[\tilde{R} - 2\partial_\mu\chi\partial^\mu\chi - \frac{1}{2}e^{4\chi}\partial_\mu\xi\partial^\mu\xi + e^{-2\chi}F_{\mu\nu}F^{\mu\nu} + \xi F_{\mu\nu}\tilde{F}^{\mu\nu}\Big], \tag{1}$$

where $\tilde{R}$ is the Ricci scalar, $F_{\mu\nu}$ is the second-order antisymmetric Maxwell field strength tensor with $F_{\mu\nu} = \nabla_\mu A_\nu - \nabla_\nu A_\mu$, and $\tilde{F}^{\mu\nu}$ is the dual tensor of the field strength. The variation of the aforementioned four fields yields the following motion equations:

$$\begin{aligned}
&\Box\chi - \frac{1}{2}e^{4\chi}\nabla_\mu\xi\nabla^\mu\xi + \frac{1}{2}e^{-2\chi}F_{\mu\nu}F^{\mu\nu} = 0,\\
&\Box\xi + 4\nabla_\mu\xi\nabla^\mu\xi - e^{-4\chi}F_{\mu\nu}\tilde{F}^{\mu\nu} = 0,\\
&\nabla_\mu\tilde{F}^{\mu\nu} = 0,\\
&\nabla_\mu(e^{-2\chi}F^{\mu\nu} + \xi\tilde{F}^{\mu\nu}) = 0,\\
&G_{\mu\nu} = e^{2\chi}(4F_{\mu\rho}F^{\rho}_{\nu} - g_{\mu\nu}F^2) - g_{\mu\nu}\left(2\nabla_\mu\chi\nabla^\mu\chi + \frac{1}{2}e^{4\chi}\nabla_\mu\xi\nabla^\mu\xi\right) + \nabla_\mu\chi\nabla_\nu\chi + e^{4\chi}\nabla_\mu\xi\nabla_\nu\xi.
\end{aligned} \tag{2}$$

These equations indicate that the dilaton field, the axion field, the electromagnetic field, and the gravitational field are observed to be coupled. The classical axisymmetric solution, known as the Kerr-Sen solution, can be expressed in Boyer-Lindquist coordinates as [61–63]

$$ds^2 = -\left(1 - \frac{2Mr}{\tilde{\Sigma}}\right)dt^2 + \frac{\tilde{\Sigma}}{\tilde{\Delta}}dr^2 + \tilde{\Sigma}d\theta^2 - \frac{4aMr}{\tilde{\Sigma}}\sin^2\theta dt d\phi + \sin^2\theta d\phi^2\left(r(r+r_2) + a^2 + \frac{2Mra^2\sin^2\theta}{\tilde{\Sigma}}\right), \tag{3}$$

with

$$\begin{aligned}
\tilde{\Sigma} &= r(r+r_2) + a^2\cos^2\theta,\\
\tilde{\Delta} &= r(r+r_2) - 2Mr + a^2,
\end{aligned} \tag{4}$$

where M is the mass parameter of the black hole, the dilaton parameter is defined as $r_2 = \frac{Q^2}{M}$ (Q represents the electric charge), and a denotes the black hole's angular momentum per unit mass. Equation (3) indicates that when the black hole's rotation parameter is excluded, it results in a spherically symmetric dilaton black hole composed of mass, electric charge, and asymptotic value [64]. When the dilaton parameter r_2 vanishes, the Kerr-Sen solution reverts to the Kerr black hole.

The event horizon $r_\pm$ of the Kerr-Sen black hole is determined by

$$r_+ = M - \frac{r_2}{2} + \sqrt{\left(M - \frac{r_2}{2}\right)^2 - a^2},$$
$$r_- = M - \frac{r_2}{2} - \sqrt{\left(M - \frac{r_2}{2}\right)^2 - a^2}. \tag{5}$$

According to Eq. (5), the theoretical range of parameters within which internal and external event horizons exist can be determined as $0 \leqslant \frac{r_2}{M} \leqslant 2(1 - \frac{a}{M})$ or $-(1 - \frac{r_2}{2M}) \leqslant \frac{a}{M} \leqslant 1 - \frac{r_2}{2M}$. Since the spin parameter a cannot exceed the black hole mass M, it can be deduced that the theoretical effective range for the parameter r_2 is $0 \leqslant \frac{r_2}{M} \leqslant 2$. In the next section, we will consider a nonrelativistic, steady-state, irrotational fluid accretion process in the spacetime of a Kerr-Sen black hole.

III. ACCRETION SOLUTION FOR ULTRARELATIVISTIC PREFECT FLUID

The primary objective of this section is to investigate the ultrarelativistic perfect fluid accretion solution. Specifically, the steady-state fluid with an ultrarelativistic stiff equation of state which can be described as

$$P = K\rho^2, \tag{6}$$

where K is a constant and ρ and P are the proper mass density and the proper pressure, respectively. Since the perfect fluids satisfy the first law of thermodynamics: $\mathrm{d}h = \frac{\mathrm{d}P}{\rho}$ [65] (h represents the specific enthalpy defined as $\frac{u+P}{\rho}$ and u denotes the total energy density), substituting this expression into the aforementioned formula, we obtain

$$h = 2K\rho. \tag{7}$$

In hydromechanics, the speed of sound plays a crucial role as a fundamental physical parameter for analyzing the velocity of fluid. We derive the fluid's sound speed $c_s^2 \equiv \sqrt{\frac{\partial \ln h}{\partial \ln \rho}} = 1$, which indicates that the fluid's velocity is subsonic. The basic equations for investigating the evolution of the fluid are the continuity equation and the energy-momentum conservation equation, which have the following forms:

$$\nabla_\mu J^\mu = \nabla_\mu(\rho U^\mu) = 0,$$
$$\nabla_\mu T^{\mu\nu} = \nabla_\mu(\rho h U^\mu U^\nu + P\delta^\mu_\nu) = 0. \tag{8}$$

Then we can derive the Euler equation by combining the above two formulas with the first law

$$U^\mu \nabla_\mu(hU_\nu) + \nabla_\nu h = 0, \tag{9}$$

where $U^\mu = \frac{\mathrm{d}x^\mu}{\mathrm{d}\tau}$ is the four-velocity for fluid and satisfies $U^\mu U_\mu = -1$. The relativistic vorticity tensor is [9]

$$\omega_{\mu\nu} = \nabla_\nu(hU_\mu) - \nabla_\mu(hU_\nu). \tag{10}$$

Utilizing the projection operator $P^\mu_\nu = \delta^\mu_\nu + U^\mu U_\nu$, we project the vorticity tensor into its spatial component:

$$\tilde{\omega}_{\mu\nu} = P^\alpha_\mu P^\beta_\nu [\nabla_\beta(hU_\alpha) - \nabla_\alpha(hU_\beta)]. \tag{11}$$

Substituting (9) into the expression of (11), one can demonstrate that, for an irrotational fluid with a zero vortex tensor, hU_μ can be expressed as the gradient of the velocity potential Φ:

$$hU_\mu = \nabla_\mu \Phi. \tag{12}$$

Subsequently, the four-velocity normalization condition requires $h = \sqrt{-\nabla_\mu \Phi \nabla^\mu \Phi}$. Utilizing (8) and (12), we obtain

$$\nabla_\mu\left(\frac{\rho}{h}\nabla^\mu \Phi\right) = 0, \tag{13}$$

which is a nonlinear differential equation and can be rewritten as

$$\nabla_\mu \nabla^\mu \Phi = 0. \tag{14}$$

The issue of thermodynamics is entirely transformed into the solution of a massless scalar field with boundary conditions. Nevertheless, it is essential to note that not all solutions to the equation are physically viable: A fluid's four-velocity must be required to be timelike. Within the permissible ranges of parameters, the theoretical values for the pressure and the specific enthalpy can be obtained by calculating the solution of the field Φ.

A. The solution in Kerr-Sen spacetime

Petrich, Shapiro, and Teukolsky investigated the solution of (14) in the Kerr spacetime under the assumption that the boundary conditions were fulfilled. In this subsection, we will follow their approach in the Kerr-Sen spacetime.

The analytical expression can be expressed as

$$-\frac{\tilde{A}}{\tilde{\Delta}\tilde{\Sigma}}\partial_t^2\Phi + \frac{1}{\tilde{\Sigma}}\partial_r(\tilde{\Delta}\partial_r\Phi) + \frac{1}{\tilde{\Sigma}\sin\theta}\partial_\theta(\sin\theta\partial_\theta\Phi)$$
$$+ \frac{\tilde{\Delta} - a^2\sin^2\theta}{\tilde{\Sigma}\tilde{\Delta}\sin^2\theta}\partial_\phi^2\Phi - \frac{4Mra}{\tilde{\Delta}\tilde{\Sigma}}\partial_t\partial_\phi\Phi = 0, \tag{15}$$

where $\tilde{A}$ is defined as

$$\tilde{A} = [r(r + r_2) + a^2]^2 - a^2 \sin^2\theta\tilde{\Delta}. \tag{16}$$

According to the steady-state fluid accretion process, the solution is

$$\Phi = e\left[-t + \sum_{lm} R_{lm}(r) Y_{lm}(\theta, \phi)\right], \tag{17}$$

where the velocity potential Φ has decomposed by the standard spherical harmonics which serve as a set of complete basis. The positive e is related to the Bernoulli constant (per unit mass) and can be solved by

$$e = -hU_\mu \left(\frac{\partial}{\partial t}\right)^\mu = -\partial_t \Phi, \tag{18}$$

with the timelike Killing vector field $(\frac{\partial}{\partial t})^\mu = (1, 0, 0, 0)$. Substituting (17) back into (15), we can derive

$$\frac{\mathrm{d}}{\mathrm{d}r}[\tilde{\Delta}\partial_r R_{lm}(r)] - l(l+1)R_{lm}(r) + \frac{m^2 a^2}{\tilde{\Delta}} R_{lm}(r) = 0. \tag{19}$$

To simplify the radial component of (19), we introduce a new variable z to transform the equation for $R_{lm}(r)$ into the Legendre equation:

$$z \equiv \frac{r - M + \frac{r_2}{2}}{\sqrt{(M - \frac{r_2}{2})^2 - a^2}},$$

$$(1 - z^2)\frac{\mathrm{d}^2}{\mathrm{d}z^2} R_{lm}(z) - 2z\frac{\mathrm{d}}{\mathrm{d}z} R_{lm}(z) + l(l+1)R_{lm}(z) - \frac{(i\alpha m)^2}{1 - z^2} R_{lm}(z) = 0. \tag{20}$$

Following this, Eq. (17) can be formulated in a general form:

$$\Phi = e\left[-t + \sum_l (A_l P_l(z) + B_l Q_l(z)) Y_{l0} + \sum_{lm} (A^+_{lm} P^{im\alpha}_l(z) + A^-_{lm} P^{-im\alpha}_l(z)) Y_{lm}(\theta, \phi)\right], \tag{21}$$

where $\alpha \equiv \frac{a}{\sqrt{(M - \frac{r_2}{2})^2 - a^2}}$, m is a positive integer, and coefficients A_l, B_l, A^+_{lm}, and A^-_{lm} could be determined by boundary conditions. $P_l(z)$, $P^{im\alpha}_l(z)$, and $Q_l(z)$ are Legendre functions of the first and the second kind. $P^{im\alpha}_l(z)$ can be described as a hypergeometric function [66]:

$$P^{im\alpha}_l(z) \propto \mathrm{e}^{imX} F\left(-l, l+1, 1 - im\alpha; \frac{1 - z}{2}\right),$$

$$X \equiv \frac{\alpha}{2} \ln\frac{z+1}{z-1} = \frac{a}{2\sqrt{(M - \frac{r_2}{2})^2 - a^2}} \ln\frac{r - r_-}{r - r_+}. \tag{22}$$

Using Eq. (12) and the normalization condition for the four-velocity, we obtain

$$hU_t = -e,$$

$$hU_r = \frac{e[\sum_l (A_l P'_l(z) + B_l Q'_l(z)) Y_{l0}(\theta, \phi) + \sum_{lm} (A^+_{lm} P'^{im\alpha}_l(z) + A^-_{lm} P'^{-im\alpha}_l(z)) Y_{lm}(\theta, \phi)]}{\sqrt{(M - \frac{r_2}{2})^2 - a^2}},$$

$$hU_\theta = e\left[\sum_l (A_l P_l(z) + B_l Q_l(z)) \frac{\partial Y_{l0}(\theta, \phi)}{\partial\theta} + \sum_{lm} (A^+_{lm} P^{im\alpha}_l(z) + A^-_{lm} P^{-im\alpha}_l(z)) \frac{\partial Y_{lm}(\theta, \phi)}{\partial\theta}\right],$$

$$hU_\phi = e\left[\sum_{lm} (A^+_{lm} P^{im\alpha}_l(z) + A^-_{lm} P^{-im\alpha}_l(z)) \frac{\partial Y_{lm}(\theta, \phi)}{\partial\phi}\right], \tag{23}$$

with

$$h^2=\frac{1}{\tilde{\Delta}\tilde{\Sigma}}\left[e^2\tilde{A}-\tilde{\Delta}^2(hU_r)^2-\tilde{\Delta}(hU_\theta)^2-\frac{\tilde{\Delta}-a^2\sin^2\theta}{\sin^2\theta}(hU_\phi)^2+4Mrae(hU_\phi)\right]. \tag{24}$$

The prime denotes the derivative with respect to z and the analytical solution reveals a physical constraint: It must remain finite at r_+, necessitating A^+_{lm} to be 0 (since $P^{im\alpha}_l$ is divergent at $r+$). Employing the limiting behavior as $z\to 1$ (corresponding to $r\to r+$), we have

$$h^2\to\frac{[r_+(r_++r_2)+a^2]^2e^2-\left[\sqrt{(M-\frac{r_2}{2})^2-a^2}\sum_l B_l Y_{lm}(\theta,\phi)\right]^2}{\tilde{\Delta}(r_+)\tilde{\Sigma}(r_+)}. \tag{25}$$

Analyzing the specific enthalpy with a focus on its continuity at the horizon, we conclude that only B_0 contributes, and the other terms $B_l(l>0)$ vanish. This implies that

$$B_0=\frac{e[r_+(r_++r_2)+a^2]}{\sqrt{(M-\frac{r_2}{2})^2-a^2}}, \tag{26}$$

where Y_{00}'s contribution is absorbed into B_0. By using the formula $Q_0(x)=\frac{1}{2}\ln\frac{1+x}{1-x}$, the associated solution degenerates to

$$\begin{aligned}\Phi&=e[-t+\psi(r,\theta,\phi)],\\ \psi(r,\theta,\phi)&\equiv\frac{r_+(r_++r_2)+a^2}{2\sqrt{(M-\frac{r_2}{2})^2-a^2}}\ln\frac{r-r_-}{r-r_+}\\ &\quad+\sum_{l,m\geq 0}A^-_{lm}e^{-im\chi}F\left(-l,l+1;1+im\alpha;\frac{1-z}{2}\right)\\ &\quad\times Y_{lm}(\theta,\phi).\end{aligned} \tag{27}$$

Since Φ is a real scalar field, a constraint is imposed: $A^-_{l-m}=(-1)^m(A^-_{lm})^*$. In the study of steady-state accretion scenarios, it is common to assume an axisymmetric fluid distribution and a reflection symmetry about the equatorial plane. This allows us to focus on only modes with $m=0$, and the angular quantum number l must be an even integer. The coefficients A^-_{lm} correspond to the distinctive structure of the fluid, and its determination will be addressed subsequently.

Equations (12), (23), and (27) give the exact analytical formulas for U^μ and the specific enthalpy, which yields

$$\begin{aligned}\frac{hU^t}{e}&=\frac{\tilde{A}}{\tilde{\Delta}\tilde{\Sigma}}-\frac{2Mra}{\tilde{\Delta}\tilde{\Sigma}}\partial_\phi\psi,\\ \frac{hU^r}{e}&=\frac{\tilde{\Delta}}{\tilde{\Sigma}}\partial_r\psi,\\ \frac{hU^\theta}{e}&=\frac{1}{\tilde{\Sigma}}\partial_\theta\psi,\\ \frac{hU^\phi}{e}&=\frac{2Mra}{\tilde{\Delta}\tilde{\Sigma}}+\frac{\tilde{\Delta}-a^2\sin^2\theta}{\tilde{\Delta}\tilde{\Sigma}\sin^2\theta}\partial_\phi\psi,\end{aligned} \tag{28}$$

and

$$\begin{aligned}\frac{h^2}{e^2}&=\frac{\tilde{A}}{\tilde{\Delta}\tilde{\Sigma}}-\frac{\tilde{\Delta}}{\tilde{\Sigma}}(\partial_r\psi)^2-\frac{1}{\tilde{\Sigma}}(\partial_\theta\psi)^2\\ &\quad-\frac{\tilde{\Delta}-a^2\sin^2\theta}{\tilde{\Delta}\tilde{\Sigma}\sin^2\theta}(\partial_\phi\psi)^2-\frac{4Mra}{\tilde{\Delta}\tilde{\Sigma}}(\partial_\phi\psi).\end{aligned} \tag{29}$$

There are two inherent constraints in (28) and (29): The first constraint is that the right-hand side of Eq. (29) must be positive, as the four-velocity U^μ is required to be timelike. It is evident that not every point r in Kerr-Sen spacetime satisfies this criteria.

Nevertheless, this issue can be addressed by selecting A^-_{lm} small enough to ensure that h is well defined within the spherical shell's interval $r_+\leqslant r\leqslant R$ (R is a spherical radius). The second constraint is that $U^r(r_+)<0$ for the fluid to flow radially into the event horizon. Fortunately, it can be demonstrated that this condition is automatically satisfied by the accretion solution of the ultrarelativistic fluid.

B. Mass accretion rate for ultrarelativistic stiff fluid

The accretion rate of a black hole is one of the most significant concepts in astronomy. It is derived from the mass conservation flow and describes how rapidly the black hole absorbs surrounding fluids. The constraint from stationary accretion is internally consistent with the following conditions: (i) the accreted matter is light-weight fluid, and (ii) the growth rate of black hole mass is slow [13,67,68]. Generally speaking, based on considerations by previous researchers on black hole accretion, it can be stated that these two conditions are generally satisfied due to the difficulty of the accreted matter's mass reaching the order of the black hole's mass. Therefore, when addressing the accretion of ordinary matter from the interstellar medium onto a sufficiently massive black hole, we can neglect the impact of backreaction.

The conserved quantities of physical system are determined by the number of Killing vector fields. Given that the Kerr-Sen black hole exhibits symmetries in the t and ϕ coordinates, we can define the conservation flow

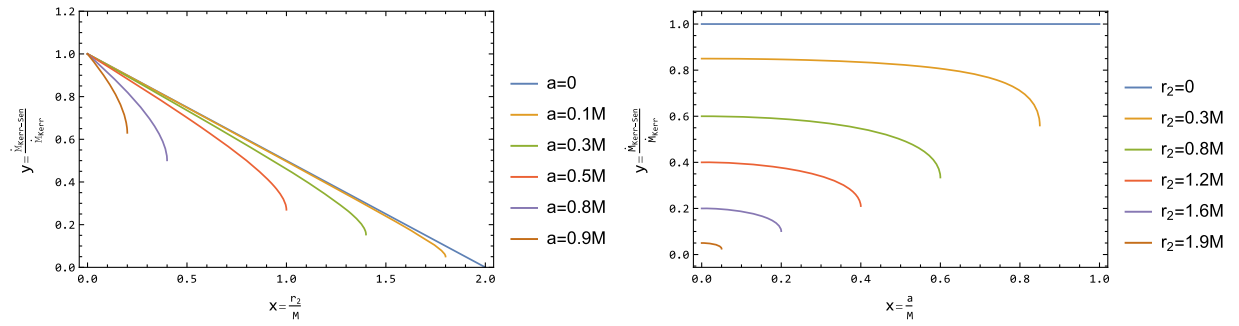

FIG. 1. The ratio of the accretion rate for the Kerr-Sen black hole to that of the Kerr black hole is illustrated with $a = 0$, 0.1, 0.3, 0.5, 0.8, 0.9 M and $r_2 = 0$, 0.3, 0.8, 1.2, 1.6, 1.9 M.

$$J^\mu_\varepsilon = -T^\mu_\nu\left(\frac{\partial}{\partial t}\right)^\nu,$$
$$J^\mu_L = T^\mu_\nu\left(\frac{\partial}{\partial \phi}\right)^\nu, \tag{30}$$

which correspond to the energy, the angular momentum, and the mass flow $J^\mu = \rho U^\mu$, respectively. Combining (12) with the stiff equation of state yields the deduced conserved current as follows:

$$J^\mu = \frac{\rho}{h}\nabla^\mu\Phi,$$
$$T^\mu_\nu = \frac{\rho}{h}\left(\nabla^\mu\Phi\nabla_\nu\Phi - \frac{1}{2}\delta^\mu_\nu\nabla_\sigma\Phi\nabla^\sigma\Phi\right). \tag{31}$$

The mass flow through the surface of a sphere with a certain radius is referred to the mass accretion rate, which yields

$$\dot{\mathcal{M}} = -\int_S J^r\sqrt{-g}\mathrm{d}\theta\mathrm{d}\phi, \tag{32}$$

with the dot denoting the time derivative and S meaning any sphere of radius r. In particular, it should be emphasized that $\dot{\mathcal{M}}$ is independent of the position chosen during the steady-state accretion process. Therefore, we select the surface $r = r_+$. In order to have an explicit expression for the accretion rate, we solve $\dot{\mathcal{M}}$ by substituting $J^r = \frac{\rho e\tilde{\Delta}}{\tilde{\Sigma}}\partial_r\psi$ and (27) into (32):

$$\dot{\mathcal{M}} = -\frac{\rho e}{h}\int_{r=r_+}\tilde{\Delta}\partial_r\psi\sin\theta\mathrm{d}\theta\mathrm{d}\phi$$
$$= \frac{4\pi\rho e}{h}[r_+(r_+ + r_2) + a^2]. \tag{33}$$

It appears that the ultrarelativistic fluid with $\frac{\rho}{h} = \frac{1}{2K}$ can be moved outside of the integral. The energy accretion rate $\dot{M}$ and angular momentum accretion rate $\dot{J}$ could be expressed as

$$\dot{M} = -\int_{r=r_+} J^r_\varepsilon\tilde{\Sigma}\sin\theta\mathrm{d}\theta\mathrm{d}\phi = e\dot{\mathcal{M}},$$
$$\dot{J} = -\int_{r=r_+} J^r_L\tilde{\Sigma}\sin\theta\mathrm{d}\theta\mathrm{d}\phi = 0. \tag{34}$$

The formulas indicate that both the mass accretion rate and energy accretion rate remain constant. The transformation of angular momentum is zero, which implies that the steady-state fluid is axisymmetric ($m = 0$) in the Boyer-Lindquist coordinate system. The ratio of the accretion rate for the Kerr-Sen black hole to that of the Kerr black hole is depicted in Fig. 1. Both figures indicate that within the theoretically permissible range of parameters, as a and r_2 increase, the accretion rate of the Kerr-Sen black hole decreases significantly, comparing with that of the Kerr black hole.

IV. THE QUADRUPOLAR FLOW SOLUTION IN ZAMO FRAMEWORK

To investigate the relative velocity in three dimensions, it is more convenient to adopt the zero angular momentum observer (ZAMO) framework [69,70]. The observer's four-velocity depends on $\frac{\partial}{\partial t} + \Omega\frac{\partial}{\partial\phi}$ ($\Omega = \frac{2Mar}{\tilde{A}}$ is the angular velocity). On the background of the Kerr-Sen black hole, the four orthogonal basis vectors could be expressed as

$$e_{\hat{t}} = \sqrt{\frac{\tilde{A}}{\tilde{\Sigma}\tilde{\Delta}}}(1,0,0,\Omega), \qquad e_{\hat{r}} = \sqrt{\frac{\tilde{\Delta}}{\tilde{\Sigma}}}(0,1,0,0),$$
$$e_{\hat{\theta}} = \frac{1}{\sqrt{\tilde{\Sigma}}}(0,0,1,0), \qquad e_{\hat{\phi}} = \sqrt{\frac{\tilde{\Sigma}}{\tilde{A}\sin^2\theta}}(0,0,0,1). \tag{35}$$

According to the coordinate transformational relation $U^{\hat{\mu}} = e^{\hat{\mu}}_\beta U^\beta$, the four-velocities within ZAMO framework are

$$\frac{h}{e}U^{\hat{t}} = \sqrt{\frac{\tilde{A}}{\tilde{\Sigma}\tilde{\Delta}}}(1-\Omega\partial_\phi\psi), \qquad \frac{h}{e}U^{\hat{r}} = \sqrt{\frac{\tilde{\Delta}}{\tilde{\Sigma}}}\partial_r\psi,$$
$$\frac{h}{e}U^{\hat{\theta}} = \frac{1}{\sqrt{\tilde{\Sigma}}}\partial_\theta\psi, \qquad \frac{h}{e}U^{\hat{\phi}} = \sqrt{\frac{\tilde{\Sigma}}{\tilde{A}\sin^2\theta}}\partial_\phi\psi. \tag{36}$$

The Lorentz factor is $\Gamma \equiv U^{\hat{t}} = \frac{1}{\sqrt{1-V^2}}$, and the additional three-velocity corresponding to Eq. (36) can be defined as

$$V^{\hat{r}} = \frac{U^{\hat{r}}}{U^{\hat{t}}} = \frac{\tilde{\Delta}\partial_r\psi}{\sqrt{\tilde{A}}(1-\Omega\partial_\phi\psi)},$$
$$V^{\hat{\theta}} = \frac{U^{\hat{\theta}}}{U^{\hat{t}}} = \frac{\sqrt{\tilde{\Delta}}\partial_\theta\psi}{\sqrt{\tilde{A}}(1-\Omega\partial_\phi\psi)},$$
$$V^{\hat{\phi}} = \frac{U^{\hat{\phi}}}{U^{\hat{t}}} = \frac{\tilde{\Sigma}\sqrt{\tilde{\Delta}}\,\partial_\phi\psi}{\tilde{A}\sin\theta(1-\Omega\partial_\phi\psi)}, \tag{37}$$

with

$$V = \sqrt{(V^{\hat{r}})^2 + (V^{\hat{\theta}})^2 + (V^{\hat{\phi}})^2}. \tag{38}$$

Evidently, these representations of three- and four-velocities lead to variety of relevant conclusions. The timelike characteristic of four-velocity requires $V < 1$ ($U^{\hat{t}} > 0$). Therefore, we can constrain the three-velocity highlighted above according to the following two conditions:

$$\Omega\partial_\phi\psi < 1 \tag{39}$$

and

$$V^2 = \frac{1}{\tilde{A}(1-\Omega\partial_\phi\psi)^2}\left[(\tilde{\Delta}\partial_r\psi)^2 + \tilde{\Delta}(\partial_\theta\psi)^2 + \frac{\tilde{\Delta}\tilde{\Sigma}^2}{\tilde{A}\sin^2\theta}(\partial_\phi\psi)^2\right] < 1. \tag{40}$$

The case of $(l, m) = (2, 0)$, which is the essential solution utilized to characterize choked accretion, also constitutes the solution for the axisymmetric quadrupolar flow. This solution inherently satisfies the constraint equation (39) ($\partial_\phi\psi = 0$). The restriction imposed by (40) will be explained in more detail later. Specifically, the Bondi-Michel-type accretion corresponds to $l = 0$ and the wind accretion was accompanied by $l = 1$, both extensively explored in [71,72]. We extend hypergeometric series near the horizon and obtain quadrupolar flow's velocity potential Φ:

$$\Phi = e\left[-t + \frac{r_+(r_+ + r_2) + a^2}{2\sqrt{(M-\frac{r_2}{2})^2 - a^2}}\ln\frac{r-r_-}{r-r_+} + NF(r,\theta,\phi)\right],$$
$$F(r,\theta,\phi) = (3\cos^2\theta - 1)\left(3r^2 - 6Mr + 2M^2 + a^2 - 2Mr_2 + 3rr_2 + \frac{1}{2}r_2^2\right), \tag{41}$$

where N represents the coefficient A^-_{20}. Inserting Eq. (41) into Eqs. (36) and (37), we can derive

$$V^{\hat{r}} = \frac{\tilde{\Delta}NF_{,r} - 2Mr_+}{\sqrt{\tilde{A}}},$$
$$V^{\hat{\theta}} = \sqrt{\frac{\tilde{\Delta}}{\tilde{A}}}NF_{,\theta},$$
$$V^{\hat{\phi}} = 0, \tag{42}$$

and

$$\frac{h^2}{e^2} = \frac{\tilde{A}(1-V^2)}{\tilde{\Sigma}\tilde{\Delta}} = \frac{1}{\tilde{\Sigma}}\left[\frac{\tilde{A}}{\tilde{\Delta}} - \tilde{\Delta}\left(NF_{,r} - \frac{2Mr_+}{\tilde{\Delta}}\right)^2 - N^2F_{,\theta}^2\right], \tag{43}$$

with

$$F_{,r} = (3\cos^2\theta - 1)(6r - 6M + 3r_2),$$
$$F_{,\theta} = -6\cos\theta\sin\theta\left(3r^2 - 6Mr + 2M^2 + a^2 - 2Mr_2 + 3rr_2 + \frac{1}{2}r_2^2\right). \tag{44}$$

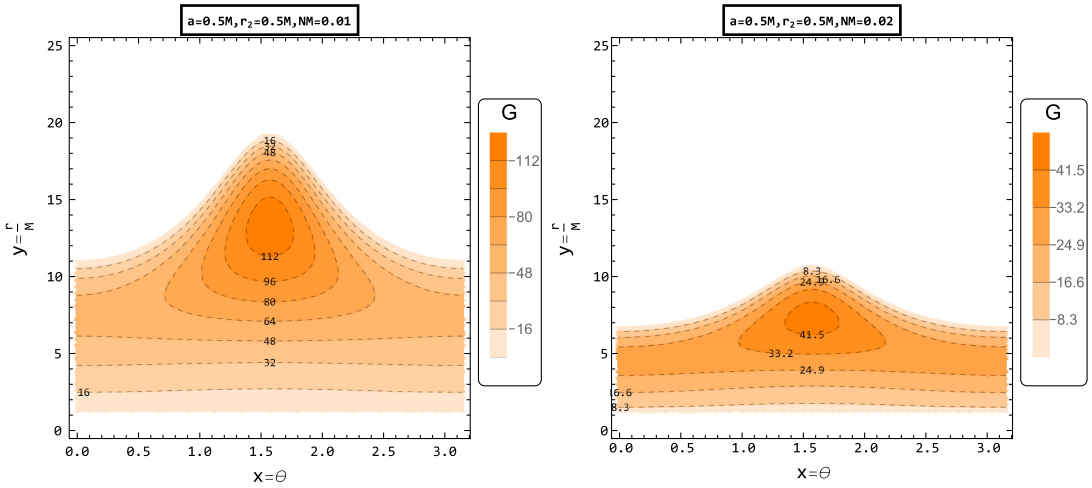

FIG. 2. The above contour maps represent G with $a = 0.5M$, $r_2 = 0.5M$, some values of N, and $NM = 0.01$ and 0.02, respectively.

The fluid distribution is entirely defined by Eq. (42). By resolving the stagnation point, we can figure out its morphological structure. The stagnation related to $V^{\hat{\theta}} = 0$ could be resolved with $\theta = 0, \frac{\pi}{2}$, and π, while $V^{\hat{r}} = 0$ will ultimately determine the location of the stagnation point. Since the flow is symmetric in the equatorial plane, there are two scenarios.

Case 1 ($\theta = 0, \pi$): $N > 0$ with inflow traveling through the equatorial plane ($\theta = \frac{\pi}{2}$) and outflow along the polar axis.—On the polar axis, the stagnation point $r = r_s$ is symmetrical distribution and fulfills

$$N = \frac{Mr_+}{(6r_s - 6M + 3r_2)(r_s - r_+)(r_s - r_-)}. \quad (45)$$

Case 2 ($\theta = \frac{\pi}{2}$): $N < 0$ is associated with inflow entering at both ends of the polar axis and outflow along the equatorial plane.—In this case, the stagnation point exists symmetrically in the equatorial plane:

$$N = -\frac{2Mr_+}{(6r_s - 6M + 3r_2)(r_s - r_+)(r_s - r_-)}. \quad (46)$$

When the black hole's parameters remain constant, the coefficients in the potential function entirely determines the location of the stationary point. In the quadrupolar flow situation, the constraint in (40) is equivalent to the positivity of the right-hand side of the last term in (43). It follows that

$$G \equiv g_0(r)\cos^4\theta + g_1(r)\cos^2\theta + g_2(r) > 0, \quad (47)$$

with

$$\begin{aligned} g_0(r) &= 9N^2(2a^2 + 4M^2 + 6r^2 + 6rr_2 + r_2^2 - 4M(3r + r_2))^2 - 9N^2(6r - 6M + 3r_2)^2\tilde{\Delta}, \\ g_1(r) &= 12NMr_+(6r - 6M + 3r_2) + 6N^2(6r - 6M + 3r_2)^2\tilde{\Delta} + a^2 \\ &\quad - 9N^2(2a^2 + 4M^2 + 6r^2 + 6rr_2 + r_2^2 - 4M(3r + r_2))^2, \\ g_2(r) &= -N^2(6r - 6M + 3r_2)^2\tilde{\Delta} - 4NMr_+(6r - 6M + 3r_2) + r^2 + rr_2 + 2Mr + 4M^2\frac{r + r_+}{r - r_-}. \end{aligned} \quad (48)$$

As the streamline is minimally influenced by the black hole parameter a, we fix $a = 0.5M$ (corresponding to the constrained range: $0 < \frac{r_2}{M} < 1$) and examine how the coefficient N affects the streamline. The physical solution relies on the four-velocity's timelike restrictions shown in the isothermal diagram Fig. 2. The horizontal axis indicates angle θ, and the vertical axis represents the dimensionless value of r. We observe that the coefficient N has an impact within the confined physical regions of parameters. The diagram becomes narrower as N increases, until there is no longer a desirable region. Therefore, the value of N must be small enough to guarantee that the requirement for the fluid

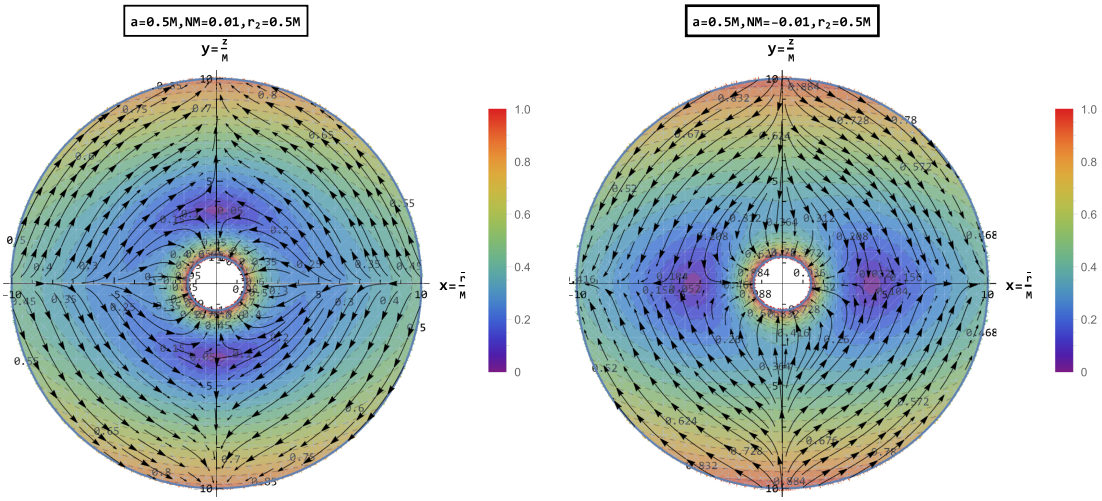

FIG. 3. Two figures correspond to the streamline (solid arrow) and the isocontour (dotted line). The magnitude of the three-velocity is entirely determined by the change in color. The diagram use cylindrical-like coordinate transformation: $\bar{r} = \sqrt{r^2 + a^2}\sin\theta$, $z = r\cos\theta$.

being timelike is satisfied within a sufficiently large radius R.

The streamline and isocontour diagram of the nonrelativistic stiff fluid determined by (42) are shown in Fig. 3. The isocontour of three-velocity are represented by the dashed line, the streamline is shown by the black arrow, and the stagnation point is symbolized by the blue area. The diagram illustrates that part of the fluid flows into the black hole, while other parts flow toward the poles or the equatorial plane. We will select $R = 10M$ as the outer radius for investigation in the following discussions, since the timelike characteristic of velocity is assured in the interval (r_+, R). It is worth noticing that the black hole domain is symbolized by the hole in the middle, which also highlights that Φ is not well defined in the ZAMO frame.

V. CHOKED ACCRETION

The choked accretion is a hydrodynamic mechanism that has been applied to the investigations of accretion onto Schwarzschild or Kerr black holes [33,34,73]. The mechanism describes that the fluid is injected radially along the equatorial plane. If the injection velocity is excessively high, the anisotropic density distribution fluctuates dramatically, leading to the deviation of part of the fluid from its original orbit and subsequent ejection along the poles. This process is reversible, as seen in cases 1 and 2, respectively. We focus on $N > 0$ (case 1) in this section.

It was mentioned previously that to fulfill the timelike requirements for four-velocity a spherical surface with a radius of R must be supplied. Physical values within the spherical shell are well defined. Simultaneously, it is crucial to establish a reference point for measuring physical quantities. The injection rate V_0 is set at $(R, \frac{\pi}{2})$ in the equatorial plane, and ejection rate V_{ej} is determined at $(R, 0)$; both can be represented as

$$V_0 = V^{\hat{r}}\left(R, \frac{\pi}{2}\right) = \frac{\tilde{\Delta}_0(6R - 6M + 3r_2)N + 2Mr_+}{\sqrt{\tilde{A}_0}},$$
$$V_{ej} = V^{\hat{r}}(R, 0) = \frac{2V_0\sqrt{\tilde{A}_0} - 6Mr_+}{R(R + r_2) + a^2}, \tag{49}$$

with

$$\tilde{\Delta}_0 = (R - r_+)(R - r_-),$$
$$\tilde{A}_0 = R(R + r_2)(a^2 + R^2 + Rr_2) + 2MRa^2. \tag{50}$$

Since the fluid is subluminal and it flows out along both ends of the polar axis, we must require $(0 < V_{ej} < 1)$ to acquire the range of the initial velocity V_0 as

$$\frac{3Mr_+}{\sqrt{\tilde{A}_0}} < V_0 < \frac{R(R + r_2) + a^2 + 6Mr_+}{2\sqrt{\tilde{A}_0}}. \tag{51}$$

Up to this point, we have not determined the stagnation point or the value of the coefficient N, in principle. Therefore, boundary constraints must be imposed. It can be concluded from (37) that

$$e = h\Gamma\sqrt{\frac{\tilde{\Sigma}\,\tilde{\Delta}}{\tilde{A}}} = h_0\Gamma_0\sqrt{\frac{\tilde{\Sigma}_0\tilde{\Delta}_0}{\tilde{A}_0}}, \tag{52}$$

where

$$\Gamma_0 = \frac{1}{\sqrt{1 - V_0^2}},$$
$$\tilde{\Sigma}_0 = R(R + r_2). \tag{53}$$

Using (7) and substituting (52) into (37), we can derive

TABLE I. The location of stagnation point, the black hole event horizon, the ratio of accretion rate, the relative density ratio, and the ejection rate are shown in the table with $a = 0.5$ M, $R = 10$ M, and $V_0 = 0.4$.

$a = 0.5$ M, $R = 10$ M, $V_0 = 0.4$										
$\frac{r_2}{M}$	0	0.1	0.2	0.3	0.4	0.5	0.6	0.7	0.8	0.9
$\frac{r_s}{M}$	4.410	4.287	4.160	4.030	3.895	3.754	3.605	3.444	3.267	3.056
$\frac{r_+}{M}$	1.866	1.758	1.648	1.537	1.425	1.310	1.190	1.065	0.932	0.780
$\frac{\dot{\mathcal{M}}_{\text{Kerr-Sen}}}{\dot{\mathcal{M}}_{\text{Kerr}}}$	1.000	0.942	0.883	0.824	0.763	0.702	0.638	0.571	0.499	0.418
V_{ej}	0.687	0.695	0.702	0.710	0.717	0.725	0.732	0.740	0.748	0.756
δ_ρ	0.479	0.492	0.504	0.517	0.529	0.541	0.554	0.566	0.579	0.594

$$\frac{h}{h_0} = \frac{\rho}{\rho_0} = \frac{\Gamma_0\sqrt{\tilde{\Sigma}_0\tilde{\Delta}_0\tilde{A}}}{\Gamma\sqrt{\tilde{\Sigma}\,\tilde{\Delta}\,\tilde{A}_0}}, \tag{54}$$

where the density $\rho_0 = \rho(R, \frac{\pi}{2})$ and the specific enthalpy $h_0 = h(R, \frac{\pi}{2})$ are determined by the parameters M, a, and r_2 with values at the reference point. According to (49), it follows that

$$N = \frac{V_0\sqrt{\tilde{A}_0} - 2Mr_+}{\tilde{\Delta}_0(6R - 6M + 3r_2)}. \tag{55}$$

Simultaneously, the two equivalent conditions (45) and (55) give the location of the stagnation point:

$$r_s = M - \frac{r_2}{2} + \left(\lambda - \sqrt{\lambda^2 - \frac{(M^2 - a^2 - Mr_2 + \frac{1}{4}r_2^2)^3}{27}}\right)^{\frac{1}{3}} + \left(\lambda + \sqrt{\lambda^2 - \frac{(M^2 - a^2 - Mr_2 + \frac{1}{4}r_2^2)^3}{27}}\right)^{\frac{1}{3}}, \tag{56}$$

with

$$\lambda \equiv \frac{Mr_+(R - r_+)(R - r_-)(R - M + \frac{r_2}{2})}{2(V_0\sqrt{\tilde{A}_0} - 2Mr_+)}. \tag{57}$$

The stagnation point, the black hole event horizon, the ratio of accretion rate, and the ejection rate are presented in Table I. The initial column in the table delineates the scenario of the Kerr black hole. The tabulated data demonstrate that the dilaton parameter r_2 increases within the range allowed by the model, and a reduction is observed in the location of the stagnation point. In contrast to this pattern, the jet ejection rate exhibits an augmentation with escalating value of the parameter.

A. Distribution of the density and the streamlines

With Eq. (54), we define a quantity δ that describes the relative deviation of the density taking the ejection's value at $(R, 0)$ from taking the injection's value at $(R, \frac{\pi}{2})$, which yields

$$\delta_\rho \equiv 1 - \frac{\rho(R,0)}{\rho(R,\frac{\pi}{2})} = 1 - \sqrt{\frac{(1 - V_{ej}^2)R(R + r_2)(R(R + r_2) + a^2)}{(1 - V_0^2)(R(R + r_2)(a^2 + R^2 + Rr_2) + 2MRa^2)}}. \tag{58}$$

We observe that the density of location $(R, 0)$ tends to zero for $\delta_\rho = 1$, while the density of the ejection point is equivalent to the injection point for $\delta_\rho = 0$. The inferences derived from the final row in Table I and Fig. 4 indicate that in the black hole an increasing parameter r_2 leads to an

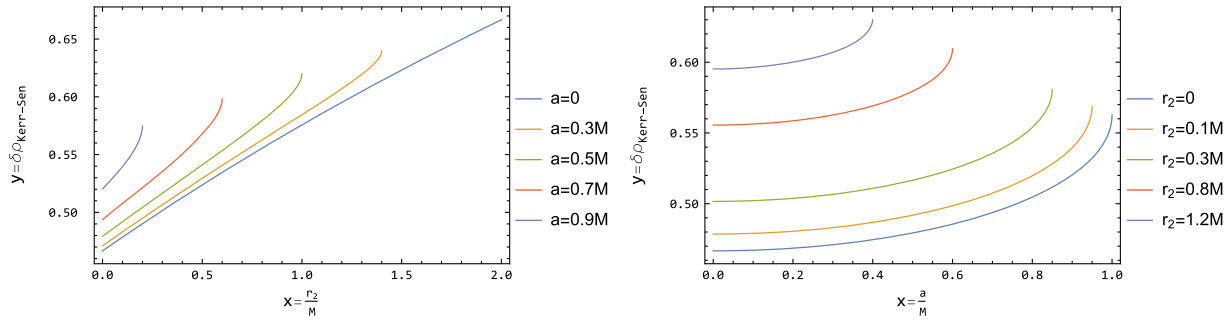

FIG. 4. The relative density ratio as a function of r_2/M (the left figure) or a/M (the right figure) with $V_0 = 0.4$, $R = 10$ M, and some values of the parameter a or r_2.

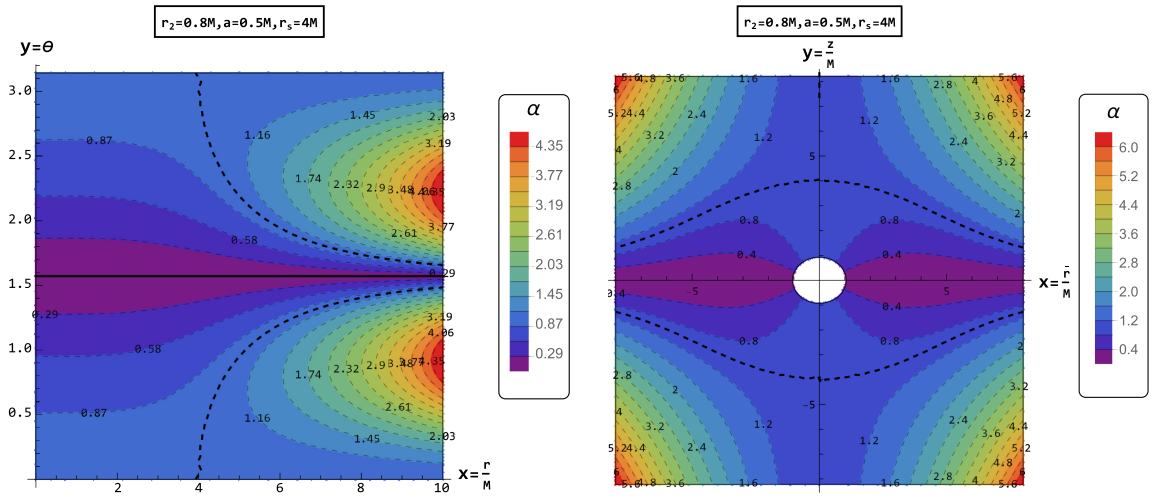

FIG. 5. For two figures: $r_2 = 0.8$ M, $a = 0.5$ M, and $r_s = 4$ M. The solid line in the left figure denotes the line with $\theta = \frac{\pi}{2}$, while the isocontour lines are represented by dashed lines. The coordinate transformations $\bar{r} = \sqrt{r^2 + a^2}\sin\theta$ and $z = r\cos\theta$ are adopted in the right figure, and the center empty region represents the interior of the Kerr-Sen black hole.

increased relative density ratio while a lower density ratio for the Kerr-Sen black hole, compared to the Kerr black hole.

Eventually, we obtain a streamlined diagram which can depict the trajectories of fluid. Applying Eq. (42) to eliminate time t, we derive

$$\alpha = \cos\theta\left[1 + \frac{\sin^2\theta(r - r_+)(r - r_-)\left(r - M + \frac{r_2}{2}\right)}{2(r_s - r_+)(r_s - r_-)\left(r_s - M + \frac{r_2}{2}\right)}\right], \tag{59}$$

where α is the constant of integration. Streamlines with $|\alpha| = 1$ are connected to the stagnation point, whereas those with $|\alpha| > 1$ escape via the bipolar outflow, and those with $|\alpha| < 1$ are absorbed into the black hole. The streamlines are described in Fig. 5. In the left diagram, we observe that the whole diagram is symmetrically distributed along the line $\theta = \frac{\pi}{2}$ (the middle solid line); the dashed lines depict the trajectories of streamline which differ from each other with different values of $|\alpha|$. It is straightforward to notice that the dividing line ($|\alpha| = 1$) indicates whether the fluid is absorbed into or ejected from the black hole. The right streamlined diagram is shown in the cylindrical-like coordinate system $(\bar{r}, z)$. Similarly, the boundary of the blue region is the line with $|\alpha| = 1$ denoted by the dotted line.

B. Injection rate, ejection rate, and critical angle

The inflow or outflow of fluid should be accompanied by the injection rate or the ejection rate, respectively. When combined with the mass accretion rate, they constitute the entire concept of choked accretion. These three rates are connected as follows:

$$\dot{\mathcal{M}}_{\rm in} = \dot{\mathcal{M}} + \dot{\mathcal{M}}_{\rm out}, \tag{60}$$

where the mass accretion rate is decided by Eq. (32). It can be described as

$$\dot{\mathcal{M}} = 8\pi M r_+ \rho_0 \Gamma_0 \sqrt{\frac{R(R + r_2)\tilde{\Delta}_0}{\tilde{A}_0}}. \tag{61}$$

For $r_2 = 0$, Eq. (61) reverts to the accretion rate of the Kerr black hole. It is obvious that the accretion rate is restricted by the parameters chosen and the bounding sphere radius R. Now we must identify the critical angle at which the fluid moves toward the black hole in the interval $(\theta_c, \pi - \theta_c)$. In this interval, the projection of the tangent vector of the streamline along the radial direction of the black hole is negative. The critical angle θ_c could be determined by using $V^{\hat{r}}$ in (42), and the flow is absorbed by the black hole with $V^{\hat{r}} < 0$; it follows that

$$\theta_c = \arccos\left[3\left(1 - \frac{2Mr_+}{V_0\sqrt{\tilde{A}_0}}\right)\right]^{-\frac{1}{2}}. \tag{62}$$

Then $\dot{\mathcal{M}}_{\rm in}$ associated with the critical angle is

$$\dot{\mathcal{M}}_{\rm in} = -2\int_{\theta_c}^{\frac{\pi}{2}} \rho U^r \tilde{\Sigma}\sin\theta \mathrm{d}\theta \mathrm{d}\phi = \frac{8\pi q \rho e M r_+}{h} = q\dot{\mathcal{M}},$$
$$q \equiv \frac{2\cos^3\theta_c}{3\cos^2\theta_c - 1} = \frac{\sqrt{\tilde{A}_0}V_0}{3\sqrt{3}Mr_+}\left(1 - \frac{2Mr_+}{V_0\sqrt{\tilde{A}_0}}\right)^{-\frac{1}{2}}. \tag{63}$$

Similarly, the ejection rate could be obtained as $\dot{\mathcal{M}}_{\rm out} = (q - 1)\dot{\mathcal{M}}$ by using (60). The physics relating to $\dot{\mathcal{M}}_{\rm in} = \dot{\mathcal{M}}$ is that all fluids are dragged into black hole while

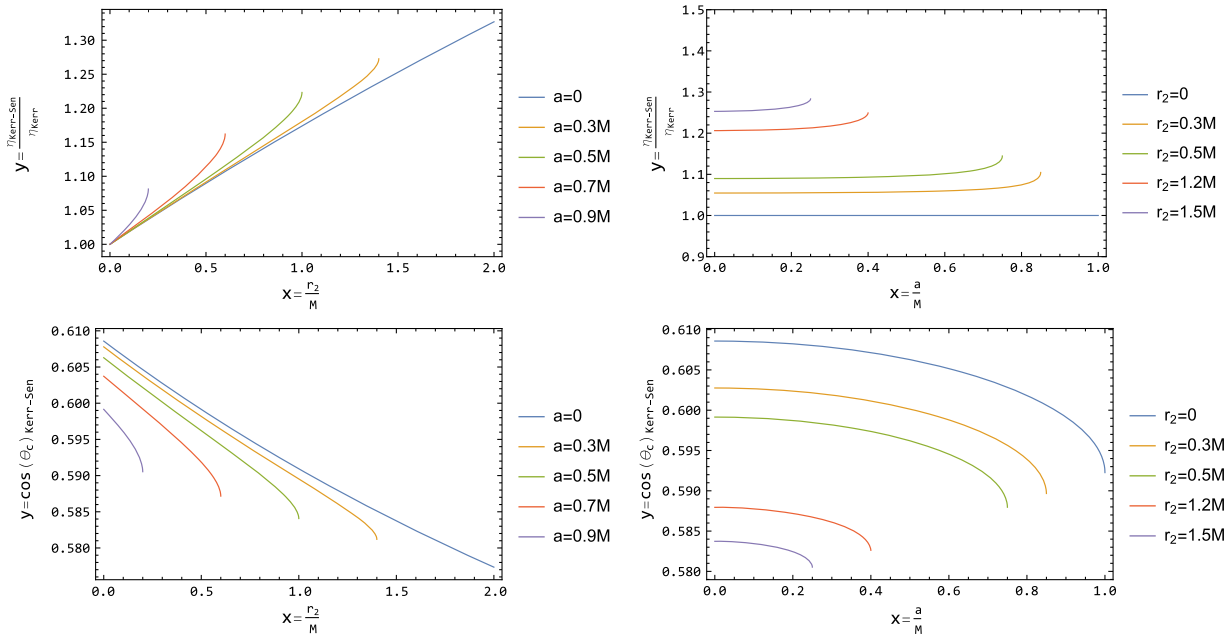

FIG. 6. For these figures: $V_0 = 0.4$ and $R = 10$ M. The figure in the upper left corner describes the evolution of η with respect to r_2, and the figure in the upper right corner illustrates the dependence of a. The critical angles with variable parameters are displayed in the lower figures.

the critical angle $\theta_c = 0$ ($q = 1$). The condition $\theta_c = 0$ provides $V_0 = \frac{3Mr_+}{\sqrt{\tilde{A}_0}}$ by (62). This is in accordance with the constraint from (51), as illustrated by the following condition:

$$\dot{\mathcal{M}}_{\text{in}} = \begin{cases} \dot{\mathcal{M}}, & V_0 \leqslant \frac{3Mr_+}{\sqrt{\tilde{A}_0}}, \\ q\dot{\mathcal{M}}, & \frac{3Mr_+}{\sqrt{\tilde{A}_0}} \leqslant V_0 \leqslant \frac{R(R+r_2)+a^2+6Mr_+}{2\sqrt{\tilde{A}_0}}, \end{cases} \tag{64}$$

and

$$\dot{\mathcal{M}}_{\text{out}} = \begin{cases} 0, & V_0 \leqslant \frac{3Mr_+}{\sqrt{\tilde{A}_0}}, \\ (q-1)\dot{\mathcal{M}}, & \frac{3Mr_+}{\sqrt{\tilde{A}_0}} \leqslant V_0 \leqslant \frac{R(R+r_2)+a^2+6Mr_+}{2\sqrt{\tilde{A}_0}}. \end{cases} \tag{65}$$

Since the range of V_0 changes, $\dot{\mathcal{M}}_{\text{in}}$ steadily increases, leading to the maximum value $\theta_{\max}$ calculated by the formula below:

$$\frac{1}{3\cos\theta_{\max}^2} = \frac{R(R+r_2)+a^2+2Mr_+}{R(R+r_2)+a^2+6Mr_+}, \tag{66}$$

and maximum value of injection accretion rate $\dot{\mathcal{M}}_{\text{inmax}} = q_{\max}\dot{\mathcal{M}}$, where

$$q_{\max} = \frac{2\cos^3\theta_{\max}}{3\cos^2\theta_{\max} - 1}. \tag{67}$$

When R is large, the maximum angle $\theta_{\max} \approx 54.7°$ ($q_{\max} \to \infty$) corresponds to the boundary case. To

TABLE II. Assuming that $a = 0.5$ M, $R = 10$ M, and $V_0 = 0.4$, some values for the ratio of injection rate, the ejection rate, and the accretion rate, and $\cos\theta_c$, $\cos\theta_{\max}$, and $q_{\max}$ are shown in the table.

$a = 0.5$ M, $R = 10$ M, $V_0 = 0.4$										
$\frac{r_2}{M}$	0	0.1	0.2	0.3	0.4	0.5	0.6	0.7	0.8	0.9
$\frac{\dot{\mathcal{M}}_{\text{Kerr-Sen}}}{\dot{\mathcal{M}}_{\text{Kerr}}}$	1.000	0.942	0.883	0.824	0.763	0.702	0.638	0.571	0.499	0.418
$\frac{\dot{\mathcal{M}}_{in\text{Kerr-Sen}}}{\dot{\mathcal{M}}_{in\text{Kerr}}}$	1.000	1.007	1.013	1.020	1.026	1.032	1.039	1.045	1.051	1.057
$\frac{\dot{\mathcal{M}}_{out\text{Kerr-Sen}}}{\dot{\mathcal{M}}_{out\text{Kerr}}}$	1.000	1.026	1.052	1.078	1.104	1.131	1.160	1.187	1.217	1.248
$\cos\theta_c$	0.606	0.604	0.602	0.600	0.598	0.596	0.594	0.592	0.590	0.588
$\cos\theta_{\max}$	0.598	0.596	0.596	0.594	0.592	0.591	0.590	0.588	0.587	0.585
$q_{\max}$	5.950	6.322	6.748	7.240	7.820	8.513	9.368	10.463	11.956	14.267

comprehend the transformation of accretion rate ratio, we depict the ratio of accretion rate $\frac{\dot{\mathcal{M}}_{\rm out}}{\dot{\mathcal{M}}_{\rm in}} \equiv \eta$ from different black holes and $\cos\theta_c$ in Fig. 6. In Table II, we calculate some values for the ratio of injection rate, the ratio of ejection rate, the ratio of accretion rate, $\cos\theta_c$, $\cos\theta_{\rm max}$, and $q_{\rm max}$.

In Fig. 6, we illustrate the influence of the parameters r_2 and a on the accretion rate ratio for Kerr and Kerr-Sen holes. When V_0 and R are fixed, we observe that the ratio $\frac{\eta_{\rm Kerr-Sen}}{\eta_{\rm Kerr}}$ rapidly increases as r_2 grows. However, with different fixed values of the dilaton parameter r_2, we find that the variation of $\frac{\eta_{\rm Kerr-Sen}}{\eta_{\rm Kerr}}$ with respect to a is not obvious. In Table II, it also indicates that, as the parameter r_2 in the Kerr-Sen black hole increases, it amplifies the ejection rate and the injection rate and simultaneously reduces the value of the critical angle and the maximum critical angle. Consequently, this leads to most of the fluid escaping from the black hole, while a very small portion flows into the black hole.

VI. RADIATIVE EFFICIENCY AND REDSHIFT FACTOR FROM THE CONTINUUM SPECTRUM

The continuum spectrum emitted by the accretion disk around a black hole is responsive to the background metric, providing a scheme for observing the Kerr-Sen black hole. In this section, we will calculate the radiative efficiency and the redshift factor from the accretion disk within the permissible interval $0 < \frac{r_2}{M} < 0.4$. This analysis will allow us to investigate the observable effect of the Kerr-Sen black hole and provide a approach to differentiate it from the Kerr black hole. We use the fundamental feature of the Novikov-Thorne model [74] provided for delineating the continuum spectrum. The model incorporates several key assumptions: (i) The primary contribution to the continuum spectrum arises from the electromagnetic emission originating from the accretion disk surrounding the black hole; (ii) the spacetime around the central massive object is both stationary and axisymmetric; (iii) the mass of the accretion disk does not influence the background metric; (iv) the accretion disk is characterized as geometrically thin, and vertical size is considered negligible compared to its horizontal size; (v) particles around the compact central object traverse between the outer edge ($r_{\rm out}$) and the radius of the innermost stable circular orbit ($r_{\rm isco}$) defined as the inner edge of the disk; and (vi) the accretion disk is situated in the equatorial plane of the accreting compact object, namely, the spin of the black hole perpendicular to the disk surface.

The innermost stable circular orbit radius can be determined from the effective potential $V_{\rm eff}$ [74,75]. For a black hole, the effective potential takes the form

$$V_{\rm eff} = \frac{E^2 g_{\phi\phi} + 2EL g_{t\phi} + L^2 g_{tt}}{g_{t\phi}^2 - g_{tt} g_{\phi\phi}}, \tag{68}$$

where E and L are the specific energy and the specific angular momentum of the test particle, respectively, and they can be calculated with the following formulas:

$$E = \frac{-g_{tt} - \omega g_{t\phi}}{\sqrt{-g_{tt} - 2\omega g_{t\phi} - \omega^2 g_{\phi\phi}}},$$
$$L = \frac{g_{t\phi} + \omega g_{\phi\phi}}{\sqrt{-g_{tt} - 2\omega g_{t\phi} - \omega^2 g_{\phi\phi}}}, \tag{69}$$

where the angular velocity of the test particle ω in the equatorial plane ($\theta = \frac{\pi}{2}$) is

$$\omega = \frac{{\rm d}\phi}{{\rm d}t} = \frac{-g_{t\phi,r} \pm \sqrt{(-g_{t\phi,r})^2 - g_{\phi\phi,r} g_{tt,r}}}{g_{\phi\phi,r}}. \tag{70}$$

The radius of the innermost stable circular orbit $r_{\rm isco}$ corresponds to the inflection point ($V_{\rm eff} = V_{{\rm eff},r} = V_{{\rm eff},rr} = 0$) [76,77]. Consequently, the determination of $r_{\rm isco}$ from the continuum spectrum could constrain the geometry of spacetime. In particular, if we assume the background to be a Kerr black hole, this measurement can be utilized to predict the angular momentum of the black holes [78].

During the accretion process, the efficiency of matter accretion and the redshift factor are important measurement quantities. The redshift factor is associated with the alteration in frequency of a photon as it traverses from the emitting source to the observer. The maximum efficiency ϵ is determined by the specific binding energy at the marginally stable orbit $r_{\rm isco}$. These two physical quantities are given by

$$\epsilon = 1 - E_{\rm isco}(r_{\rm isco}),$$
$$g \equiv 1 + z = \frac{1 - \omega r_d \sin\phi \sin\gamma}{\sqrt{-g_{tt}(r_d) - 2\omega(r_d) g_{t\phi}(r_d) - \omega^2(r_d) g_{\phi\phi}(r_d)}}, \tag{71}$$

where $E_{\rm isco}$ is the specific energy of the test particle at $r_{\rm isco}$. The parameters γ and r_d represent the inclination angle of the accretion disk and the distance from the observer to the disk, respectively. The variation of these quantities with parameters are illustrated in Fig. 7. The upper two figures illustrate the variation in radiative efficiency ϵ with the dilaton parameter r_2 (or spin parameter a) for different values of a (or r_2). The lower figures explain the variations in redshift z with the observational distance with different values of the parameters.

In Fig. 7, we observe that the radiative efficiency of the Kerr-Sen black hole increases as the parameter r_2 (or the parameter a) grows, while the redshift decreases with an

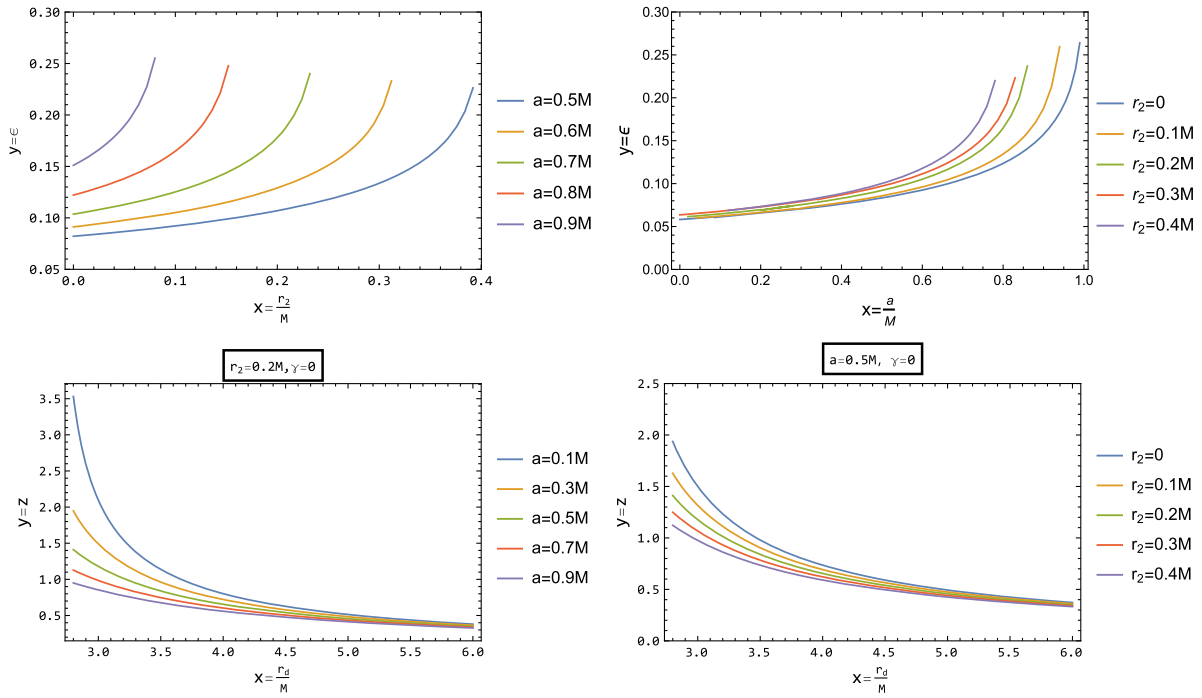

FIG. 7. The upper figures illustrate the variation of the radiative efficiency theoretically derived from the accretion disk. The lower figures illustrate the variation of redshift z with observational distance at $r_2 = 0.2$ M (or $a = 0.5$ M) under an inclination angle of $\gamma = 0$.

increasing observational distance. Furthermore, it is observed that the radiative efficiency of the Kerr-Sen black hole exceeds that of the Kerr black hole with fixed parameter a, and the redshift is lower compared to the Kerr black hole. This insight will enhance our understanding of these two black holes through observations.

VII. CONCLUSION AND DISCUSSION

In this work, we initially explored the choked accretion process of ultrarelativistic fluid onto an axisymmetric Kerr-Sen black hole in EMDA gravity. Based on the procedure mentioned by Petrich, Shapiro, and Teukolsky, we calculated the solution describing the velocity potential field Φ of a stationary, irrotational ultrarelativistic fluid in the Boyer-Lindquist coordinates system. We discussed the analytical expression of four-velocity and converted it to the ZAMO framework to give three-velocity. The mass accretion rate, the energy accretion rate, and the angular momentum increase rate were also determined. We found that the increase rate of the angular momentum is zero, indicating that the fluid has an axisymmetric distribution ($m = 0$).

Second, as a result of the axial symmetry of perfect fluid and the reflection symmetry in the equatorial plane, we gave the lowest-order (2,0) solution, commonly known as quadrupolar flow. We investigated the character of quadrupolar flow and demonstrated that one of the two constraints is automatically satisfied and the timelike requirement of the four-velocity is also resolved once an appropriate region is chosen. Subsequently, we examined the correlation between dilaton parameters r_2 and stagnation point r_s. From the table, it is evident that an increasing dilaton parameter leads to a decreasing position of the stationary point of the Kerr-Sen black hole. Then, we introduced the choked accretion model and restricted the physical region as (r_+, R) to ensure that the solution is reasonable. We also calculated the stagnation point analytic formulas based on the boundary values. Within the permissible range of the parameters, the initial velocity V_0 at the reference point enables us to depict its dependency on the parameters. The connection between the density ratio at the end point and at the initial point was also evaluated. Additionally, we presented the streamline diagram in cylindrical-like coordinates and discovered that the streamline associated with $\alpha \leqslant 1$ indicates that the fluid was absorbed into the black hole, whereas the streamline with $\alpha > 1$ represents the flow ejected along poles. The injection rate and the ejection rate were discussed in detail at the end of the article. It also indicates that, as the parameter r_2 in the Kerr-Sen black hole increases, both the ejection rate and the injection rate are amplified.

Finally, we explored the accretion process in a thin disk around the Kerr-Sen black hole by employing the Novikov-Thorne model. Our study focused on analyzing the radiative efficiency and the redshift factor. The results highlight the impact of the dilaton parameter r_2 and the spin parameter a on the radiative efficiency and the redshift

within the framework of the EMDA model. These results will also contribute to exploring and distinguishing a Kerr-Sen black hole from a Kerr black hole through observations.

In future work, we will try to solve the choked accretion issue of curled fluid numerically and provide numerical results by merging it with the equation of motion with boundary via the coupling between spacetime and matter field. We will consider the reaction of matter and explore the full accretion issue for dark energy or dark matter as accreted fluid.

ACKNOWLEDGMENTS

This study is supported in part by National Natural Science Foundation of China (Grant No. 12333008) and Hebei Provincial Natural Science Foundation of China (Grant No. A2021201034).

[1] Marek A. Abramowicz and P. Chris Fragile, Foundations of black hole accretion disk theory, Living Rev. Relativity **16**, 1 (2013).
[2] F. Hoyle and R. A. Lyttleton, The evolution of the stars, Math. Proc. Cambridge Philos. Soc. **35**, 592 (1939).
[3] F. Hoyle and R. A. Lyttleton, On the physical aspects of accretion by stars, Math. Proc. Cambridge Philos. Soc. **36**, 424 (1940).
[4] F. Hoyle and R. A. Lyttleton, On the accretion of interstellar matter by stars, Math. Proc. Cambridge Philos. Soc. **36**, 325 (1940).
[5] F. Hoyle and R. A. Lyttleton, On the accretion theory of stellar evolution, Mon. Not. R. Astron. Soc. **101**, 227 (1941).
[6] H. Bondi and F. Hoyle, On the mechanism of accretion by stars, Mon. Not. R. Astron. Soc. **104**, 273 (1944).
[7] H. Bondi, On spherically symmetrical accretion, Mon. Not. R. Astron. Soc. **112**, 195 (1952).
[8] F. Curtis Michel, Accretion of matter by condensed objects, Astrophys. Space Sci. **15**, 153 (1972).
[9] Loren I. Petrich, Stuart L. Shapiro, and Saul A. Teukolsky, Accretion onto a moving black hole: An exact solution, Phys. Rev. Lett. **60**, 1781 (1988).
[10] Patryk Mach and Andrzej Odrzywo, Accretion of dark matter onto a moving Schwarzschild black hole: An exact solution, Phys. Rev. Lett. **126**, 101104 (2021).
[11] Patryk Mach and Andrzej Odrzywołek, Accretion of the relativistic Vlasov gas onto a moving Schwarzschild black hole: Exact solutions, Phys. Rev. D **103**, 024044 (2021).
[12] Ziqiang Cai and Rong-Jia Yang, Accretion of the Vlasov gas onto a Schwarzschild-like black hole, Phys. Dark Universe **42**, 101292 (2023).
[13] Edward Malec, Fluid accretion onto a spherical black hole: Relativistic description versus Bondi model, Phys. Rev. D **60**, 104043 (1999).
[14] E. Babichev, V. Dokuchaev, and Yu. Eroshenko, Black hole mass decreasing due to phantom energy accretion, Phys. Rev. Lett. **93**, 021102 (2004).
[15] Lei Jiao and Rong-Jia Yang, Accretion onto a Kiselev black hole, Eur. Phys. J. C **77**, 356 (2017).
[16] Apratim Ganguly, Sushant G. Ghosh, and Sunil D. Maharaj, Accretion onto a black hole in a string cloud background, Phys. Rev. D **90**, 064037 (2014).
[17] Rongjia Yang, Quantum gravity corrections to accretion onto a Schwarzschild black hole, Phys. Rev. D **92**, 084011 (2015).
[18] Jose A. Font, Jose M. Ibanez, and Philippos Papadopoulos, Nonaxisymmetric relativistic Bondi-Hoyle accretion onto a Kerr black hole, Mon. Not. R. Astron. Soc. **305**, 920 (1999).
[19] Rongjia Yang, Constraints from accretion onto a Tangherlini–Reissner–Nordstrom black hole, Eur. Phys. J. C **79**, 367 (2019).
[20] V. I. Parev, Hydrodynamic accretion onto rapidly rotating Kerr black hole, Mon. Not. R. Astron. Soc. **283**, 1264 (1996).
[21] Tiziana Di Matteo, Steven W. Allen, Andrew C. Fabian, Andrew S. Wilson, and Andrew J. Young, Accretion onto the supermassive black hole in M87, Astrophys. J. **582**, 133 (2003).
[22] Sergiy Silich, Guillermo Tenorio-Tagle, and Filiberto Hueyotl-Zahuantitla, Spherically-symmetric accretion onto a black hole at the center of a young stellar cluster, Astrophys. J. **686**, 172 (2008).
[23] Rodrigo Gil-Merino, Luis J. Goicoechea, Vyacheslav N. Shalyapin, and Vittorio F. Braga, Accretion onto the supermassive black hole in the high-redshift radio-loud AGN 0957 + 561, Astrophys. J. **744**, 47 (2012).
[24] C. Y. Kuo *et al.*, Measuring mass accretion rate onto the supermassive black hole in M87 using Faraday rotation measure with the submillimeter array, Astrophys. J. Lett. **783**, L33 (2014).
[25] Tong-Yu He, Ziqiang Cai, and Rong-Jia Yang, Thin accretion disks around a black hole in Einstein-Aether-scalar theory, Eur. Phys. J. C **82**, 1067 (2022).
[26] R. D. Blandford and D. G. Payne, Hydromagnetic flows from accretion discs and the production of radio jets, Mon. Not. R. Astron. Soc. **199**, 883 (1982).
[27] R. D. Blandford and R. L. Znajek, Electromagnetic extraction of energy from Kerr black holes, Mon. Not. R. Astron. Soc. **179**, 433 (1977).
[28] Vladimir Semenov, Sergey Dyadechkin, and Brian Punsly, Simulations of jets driven by black hole rotation, Science **305**, 978 (2004).
[29] Jonathan C. McKinney, General relativistic magnetohydrodynamic simulations of jet formation and large-scale

propagation from black hole accretion systems, Mon. Not. R. Astron. Soc. **368**, 1561 (2006).
[30] Qian Qian, Christian Fendt, and Christos Vourellis, Jet launching in resistive GR-MHD black hole–accretion disk systems, Astrophys. J. **859**, 28 (2018).
[31] M. Liska, A. Tchekhovskoy, A. Ingram, and M. van der Klis, Bardeen–Petterson alignment, jets, and magnetic truncation in GRMHD simulations of tilted thin accretion discs, Mon. Not. R. Astron. Soc. **487**, 550 (2019).
[32] X. Hernandez, P. L. Rendon, R. G. Rodriguez-Mota, and A. Capella, A hydrodynamical mechanism for generating astrophysical jets, Revista Mexicana de Astronomía y Astrofísica **50**, 23 (2014).
[33] Emilio Tejeda, Alejandro Aguayo-Ortiz, and X. Hernandez, Choked accretion onto a Schwarzschild black hole: A hydrodynamical jet-launching mechanism, Astrophys. J. **893**, 81 (2020).
[34] Alejandro Aguayo-Ortiz, Olivier Sarbach, and Emilio Tejeda, Choked accretion onto a Kerr black hole, Phys. Rev. D **103**, 023003 (2021).
[35] Lei Jiao and Rong-Jia Yang, Accretion onto a moving Reissner-Nordström black hole, J. Cosmol. Astropart. Phys. 09 (2017) 023.
[36] Rong-Jia Yang, Yinan Jia, and Lei Jiao, Exact solution for accretion onto a moving charged dilaton black hole, Eur. Phys. J. C **82**, 502 (2022).
[37] Mikhail V. Medvedev and Norman Murray, Hot settling accretion flow onto a spinning black hole, Astrophys. J. **581**, 431 (2002).
[38] Patrick Christopher Fragile and Peter Anninos, Tilted thick —disk accretion onto a Kerr black hole, Astrophys. J. **623**, 347 (2005).
[39] Jhumpa Bhadra and Ujjal Debnath, Accretion of new variable modified Chaplygin gas and generalized cosmic Chaplygin gas onto Schwarzschild and Kerr-Newman black holes, Eur. Phys. J. C **72**, 1912 (2012).
[40] Jose A. Jimenez Madrid and Pedro F. Gonzalez-Diaz, Evolution of a Kerr-Newman black hole in a dark energy universe, Gravitation Cosmol. **14**, 213 (2008).
[41] Haiyuan Feng, Miao Li, Gui-Rong Liang, and Rong-Jia Yang, Adiabatic accretion onto black holes in Einstein-Maxwell-scalar theory, J. Cosmol. Astropart. Phys. 04 (2022) 027.
[42] Roger Penrose, Gravitational collapse and space-time singularities, Phys. Rev. Lett. **14**, 57 (1965).
[43] S. W. Hawking, Breakdown of predictability in gravitational collapse, Phys. Rev. D **14**, 2460 (1976).
[44] Demetrios Christodoulou, The formation of black holes and singularities in spherically symmetric gravitational collapse, Commun. Pure Appl. Math. **44**, 339 (1991).
[45] Clifford M. Will, The confrontation between general relativity and experiment, Living Rev. Relativity **17**, 4 (2014).
[46] M. Milgrom, A modification of the Newtonian dynamics—Implications for galaxies, Astrophys. J. **270**, 371 (1983).
[47] J. Bekenstein and M. Milgrom, Does the missing mass problem signal the breakdown of Newtonian gravity?, Astrophys. J. **286**, 7 (1984).
[48] Mordehai Milgrom and Robert H. Sanders, MOND and the "Dearth of dark matter in ordinary elliptical galaxies", Astrophys. J. Lett. **599**, L25 (2003).
[49] Adam G. Riess *et al.*, Observational evidence from supernovae for an accelerating universe and a cosmological constant, Astron. J. **116**, 1009 (1998).
[50] Timothy Clifton, Pedro G. Ferreira, Antonio Padilla, and Constantinos Skordis, Modified gravity and cosmology, Phys. Rep. **513**, 1 (2012).
[51] X. Hernandez, V. Verteletskyi, L. Nasser, and A. Aguayo-Ortiz, Statistical analysis of the gravitational anomaly in Gaia wide binaries, Mon. Not. R. Astron. Soc. **528**, 4720 (2024).
[52] Kyu-Hyun Chae, Robust evidence for the breakdown of standard gravity at low acceleration from statistically pure binaries free of hidden companions, Astrophys. J. **960**, 114 (2024).
[53] Marek Rogatko, Positivity of energy in Einstein-Maxwell axion dilaton gravity, Classical Quantum Gravity **19**, 5063 (2002).
[54] Ashoke Sen, Rotating charged black hole solution in heterotic string theory, Phys. Rev. Lett. **69**, 1006 (1992).
[55] Riccardo Catena and Jan Moller, Axion-dilaton cosmology and dark energy, J. Cosmol. Astropart. Phys. 03 (2008) 012.
[56] Julian Sonner and Paul K. Townsend, Recurrent acceleration in dilaton-axion cosmology, Phys. Rev. D **74**, 103508 (2006).
[57] Indrani Banerjee, Bhaswati Mandal, and Soumitra SenGupta, Implications of Einstein–Maxwell dilaton–axion gravity from the black hole continuum spectrum, Mon. Not. R. Astron. Soc. **500**, 481 (2020).
[58] Siddharth Kumar Sahoo, Neeraj Yadav, and Indrani Banerjee, Imprints of Einstein-Maxwell dilaton-axion gravity in the observed shadows of Sgr A* and M87*, Phys. Rev. D **109**, 044008 (2024).
[59] Rebeca Fernández Fernández, Riccardo Della Monica, and Ivan de Martino, Constraining an Einstein-Maxwell-dilaton-axion black hole at the Galactic center with the orbit of the S2 star, J. Cosmol. Astropart. Phys. 08 (2023) 039.
[60] Bruce A. Campbell, Nemanja Kaloper, Richard Madden, and Keith A. Olive, Physical properties of four-dimensional superstring gravity black hole solutions, Nucl. Phys. **B399**, 137 (1993).
[61] A. Garcia, D. Galtsov, and O. Kechkin, Class of stationary axisymmetric solutions of the Einstein-Maxwell dilaton—axion field equations, Phys. Rev. Lett. **74**, 1276 (1995).
[62] A. M. Ghezelbash and H. M. Siahaan, Hidden and generalized conformal symmetry of Kerr-Sen spacetimes, Classical Quantum Gravity **30**, 135005 (2013).
[63] Canisius Bernard, Stationary charged scalar clouds around black holes in string theory, Phys. Rev. D **94**, 085007 (2016).
[64] David Garfinkle, Gary T. Horowitz, and Andrew Strominger, Charged black holes in string theory, Phys. Rev. D **43**, 3140 (1991); **45**, 3888(E) (1992).
[65] José A. Font, An introduction to relativistic hydrodynamics, J. Phys. Conf. Ser. **91**, 012002 (2007).
[66] E. Babichev, S. Chernov, V. Dokuchaev, and Yu. Eroshenko, Ultra-hard fluid and scalar field in the Kerr-Newman metric, Phys. Rev. D **78**, 104027 (2008).

[67] Rahul Kumar and Sushant G. Ghosh, Accretion onto a noncommutative geometry inspired black hole, Eur. Phys. J. C **77**, 577 (2017).
[68] Janusz Karkowski, Bogusz Kinasiewicz, Patryk Mach, Edward Malec, and Zdobyslaw Swierczynski, Universality and backreaction in a general-relativistic accretion of steady fluids, Phys. Rev. D **73**, 021503 (2006).
[69] Andrei V. Frolov and Valeri P. Frolov, Rigidly rotating zero-angular-momentum observer surfaces in the Kerr spacetime, Phys. Rev. D **90**, 124010 (2014).
[70] Yi Liao, Xiao-Bo Gong, and Jian-Sheng Wu, Phase-transition theory of Kerr black holes in the electromagnetic field, Astrophys. J. **835**, 247 (2017).
[71] Vladimír Karas and Rastislav Mucha, Accretion onto a rotating compact object in general relativity, Am. J. Phys. **61**, 825 (1993).
[72] Emilio Tejeda, Incompressible wind accretion, Rev. Mex. Astron. Astrofis. **54**, 171 (2018).
[73] Alejandro Aguayo-Ortiz, Emilio Tejeda, and X. Hernandez, Choked accretion: From radial infall to bipolar outflows by breaking spherical symmetry, Mon. Not. R. Astron. Soc. **490**, 5078 (2019).
[74] I. D. Novikov and K. S. Thorne, Astrophysics and black holes, in *Les Houches Summer School of Theoretical Physics: Black Holes* (Gordon and Breach, Science Publishers, New York, 1973), pp. 343–550.
[75] Don N. Page and Kip S. Thorne, Disk-accretion onto a black hole. Time-averaged structure of accretion disk, Astrophys. J. **191**, 499 (1974).
[76] G. Abbas, Hamza Rehman, M. Usama, and Tao Zhu, Accretion disc around black hole in Einstein-SU(N) non-linear sigma model, Eur. Phys. J. C **83**, 422 (2023).
[77] Malihe Heydari-Fard, Sara Ghassemi Honarvar, and Mohaddese Heydari-Fard, Thin accretion disc luminosity and its image around rotating black holes in perfect fluid dark matter, Mon. Not. R. Astron. Soc. **521**, 708 (2023).
[78] Laura Brenneman, *Measuring Supermassive Black Hole Spins in Active Galactic Nuclei* (Springer, 2013).